IntraTomo: Self-supervised Learning-based Tomography via Sinogram Synthesis and Prediction

Guangming Zang   Ramzi Idoughi   Rui Li   Peter Wonka   Wolfgang Heidrich
KAUST

1. Implementation details

1.1. Network architecture

We show in Figure 1 the architecture of our hidden layers in the sinogram prediction module, which is composed of six layers of 256 neurons and one output layer of one neuron.
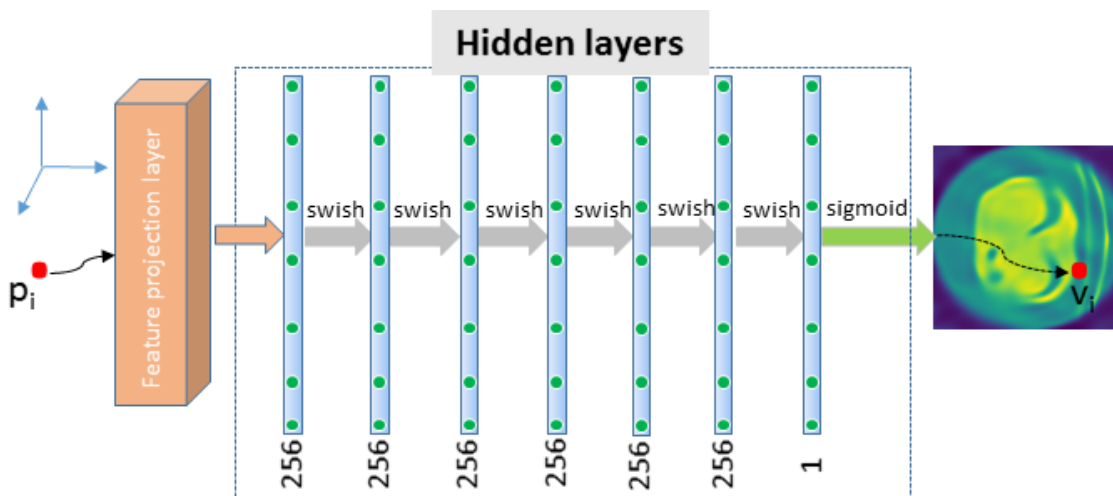

Figure 1. Architecture of the multi layer perceptron (MLP) network for the hidden layers in IntraTomo.

1.2. Parameters

The parameters used for the experiments in the main paper are shown in Table 1.

	Sparse view tomography				Limited angle tomography				Super resolution tomography		
	SL [12]	Brain [3]	ATLAS [10]	Covid-19 [7]	SL [12]	LoDoPaB [9]	Pepper	Rose	SR [2]	Pepper	Foam [4]
σ	1.5	3.0	4.0	1.8	1.5	2.8	1.8	6.0	1.5	8.0	4.0
k_1	0.1	0.1	0.05	0.2	0.15	0.15	0.1	0.1	0.05	0.05	0.1
k_2	0.15	0.15	0.18	0.2	0.2	0.2	0.2	0.2	0.1	0.2	0.2

Table 1. Parameters used in each experiment for IntraTomo

1.3. Running time

We run experiments on a single RTX 2080Ti GPU. Each method is accelerated using a CUDA backend [13]. Table 2 illustrates the obtained running time for each of the compared methods in the paper. The first experiment consists of reconstructing a 2D 256×256 density field from the Pepper dataset, using 25 sparse view projections. While the second experiment reconstructs the same density field but using a limited angle setting with 45 projections from a range of 45 degrees.

	FBP [11]	**SART** [1]	**TV** [6]	**Stochastic** [2]	**Deep prior** [5]	IntraTomo (**Ours**)
Sparse view tomography	3 seconds	1 minute	1 minute	2 minutes	14 minutes	2 minutes
Limited angle tomography	3 seconds	1 minute	2 minutes	3 minutes	32 minutes	7 minutes

Table 2. Running time for two different experiments using the Pepper dataset.

2. Supplemental results

In this section, we provide more experimental results for the datasets shown in the main paper.

2.1. Sparse view tomography

We show additional results for sparse view tomography in Figure 3 and Figure 5 (first row), with a different number of sparse views. Also, a highly undersampled case (with five views only) is evaluated, shown in Figure 2 with the SL phantom. We can observe that our method can achieve more convincing qualitative and quantitative results even in this highly ill-posed setting. Table 3 (left) shows the quantitative results for the sparse view tomography experiments in the main paper.
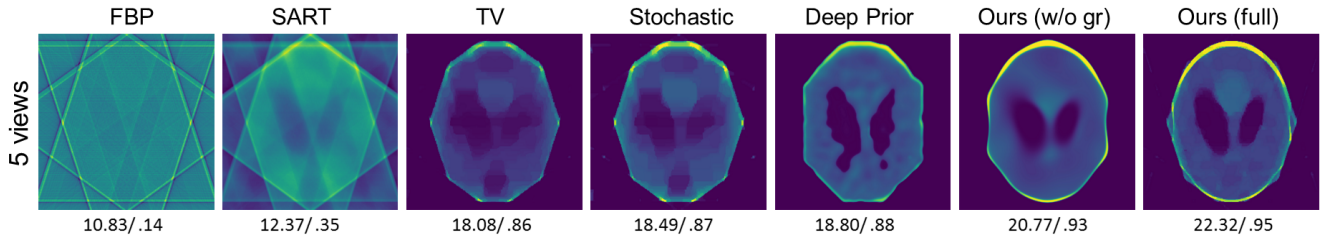

Figure 2. Sparse View tomography with 5 views for SL phantom [12] and corresponding PSNR/SSIM metrics.
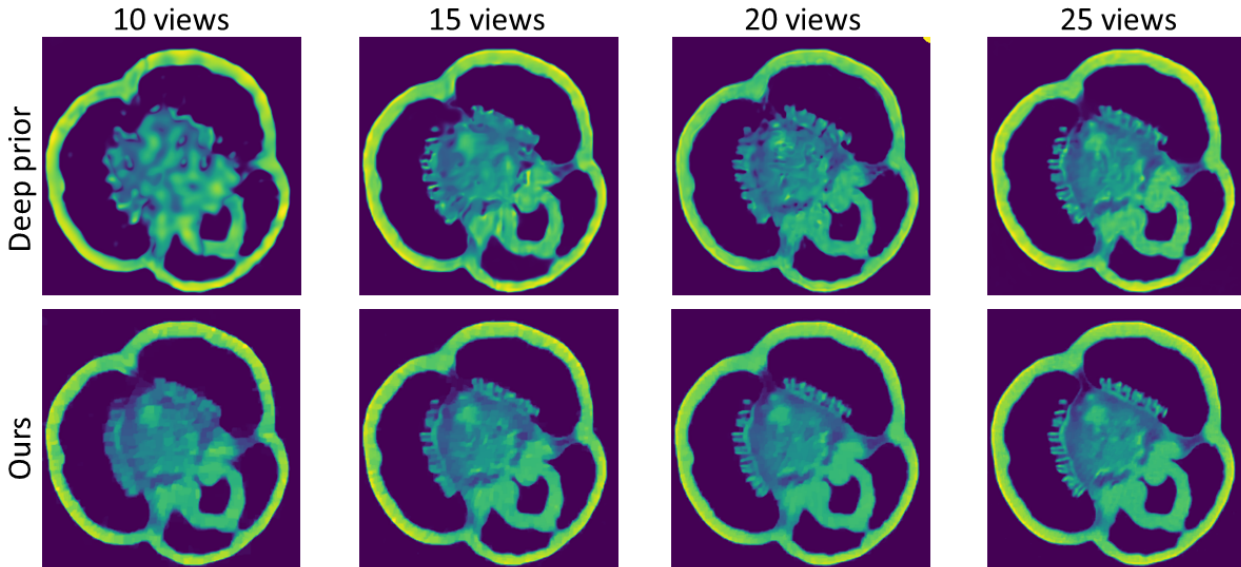

Figure 3. Sparse View tomography with 10, 15, 20, and 25 views for Deep prior (first row) [5] and Ours (second row).

2.2. Limited angle tomography

We show additional results for the limited angle tomography in Figure 4 with a different range of angles, covering 20, 30, 45, and 60 degrees. We depict a comprehensive comparison with the SOTA deep prior approach. Numerical evaluation is

shown in Table 4. Besides, Figure 5 (second row) shows with different limited angles (30, 40 and 80) for the LoDoPaB-CT dataset. Table 3 (right) shows the quantitative results for the limited angle tomography experiments in the main paper.
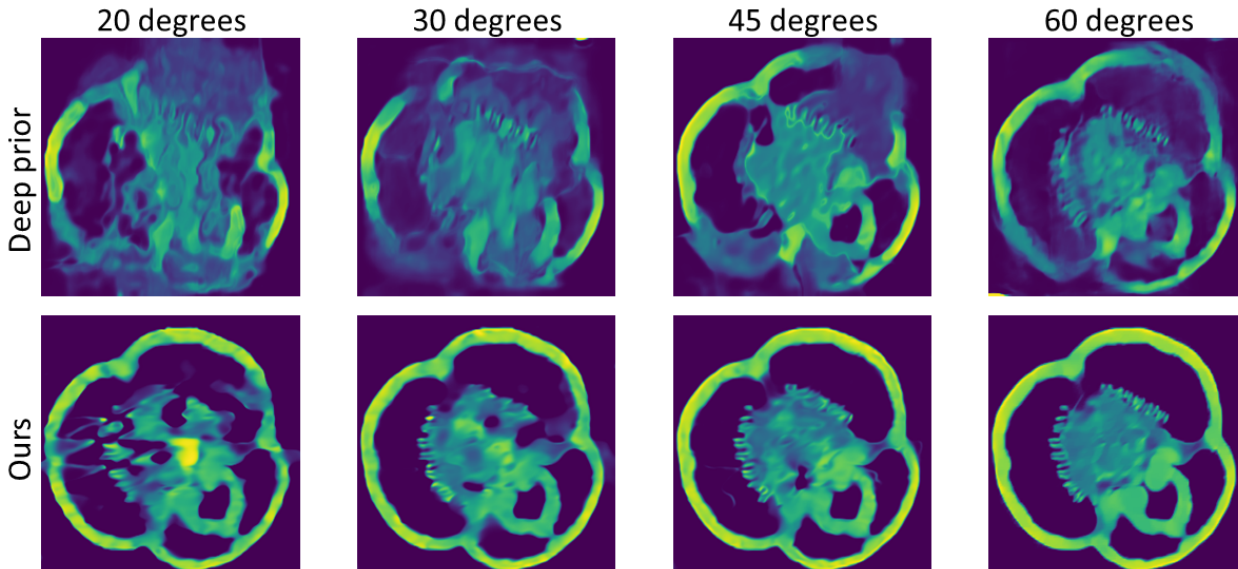

Figure 4. Limited angle tomography. The reconstruction results for Pepper dataset with 20, 30, 45, and 60 degrees respectively as input for Deep prior approach [5] (first row) and Ours (second row).

	Sparse view tomography				Limited angle tomography			
	SL [12]	Brain [3]	ATLAS [10]	Covid-19 [7]	SL [12]	LoDoPaB [9]	Pepper	Rose
FBP [11]	8.2/ .19	14.96/ .57	11.10/ .25	11.92/ .68	11.26/ .29	11.53/ .30	12.63/ .35	11.72/ .75
SART [1]	10.35/ .23	18.38/ .80	13.97/ .25	18.48/ .80	12.33/ .30	11.58/ .38	12.55/ .36	13.08/ .78
TV [6]	20.65/ .83	25.08/ .96	19.03/ .65	21.61/ .88	16.43/ .70	12.24/ .46	15.40/ .67	20.83/ .95
Stochastic [2]	21.22/ .86	25.86/ .97	19.04/ .69	22.50/ .90	16.67/ .73	12.97/ .47	15.59/ .69	21.53/ .96
Deep prior [5]	27.30/ .90	26.17/ .97	19.21/ .69	23.55/ .90	21.32/ .84	14.53/ .56	18.12/ .83	24.15/ .97
Ours (no g.r.)	28.23/ .97	26.85/ .97	18.50/ .66	24.54/ .92	26.34/ .97	20.37/ .63	25.82/ .97	29.58/ .99
Ours (full)	**28.41/ .97**	**30.38/ .99**	**22.54/ .80**	**27.19/ .95**	**26.68/ .97**	**21.80/ .69**	**28.40/ .98**	**30.06/ .99**

Table 3. PSNR/SSIM measurements for each approach. Higher values are better for PSNR and SSIM.

2.3. Super-resolution tomography

We show additional super-resolution results and analysis for the super-resolution tomography application. The Figures 6 and 7 (a scan for the blue lines of Fig. 6) show clearly that our reconstruction is much sharper than the other baseline methods, with this challenging super-resolution factor (×8). We also evaluate our super resolution application on the Foam phantom [4]. The reconstruction results are shown in Figure 8 with ×4 upsampling, while the upsampled projections with ×8 and ×16 are shown in Figure 9.

2.4. Additional comparison to baseline methods

We conduct an additional comparative study on the Pepper dataset. As shown in Table 4, different views in sparse view tomography (also see Figure 3), different angles in limited angle tomography (also see Figure 4), and different upsampling scales for the super-resolution tomography are evaluated using our method and the best selected baseline methods.

A comparison between FBP (50 views), FBPConvNet [8] (50 views) and ours with different views are provided in Figure 10 and Figure 11 .
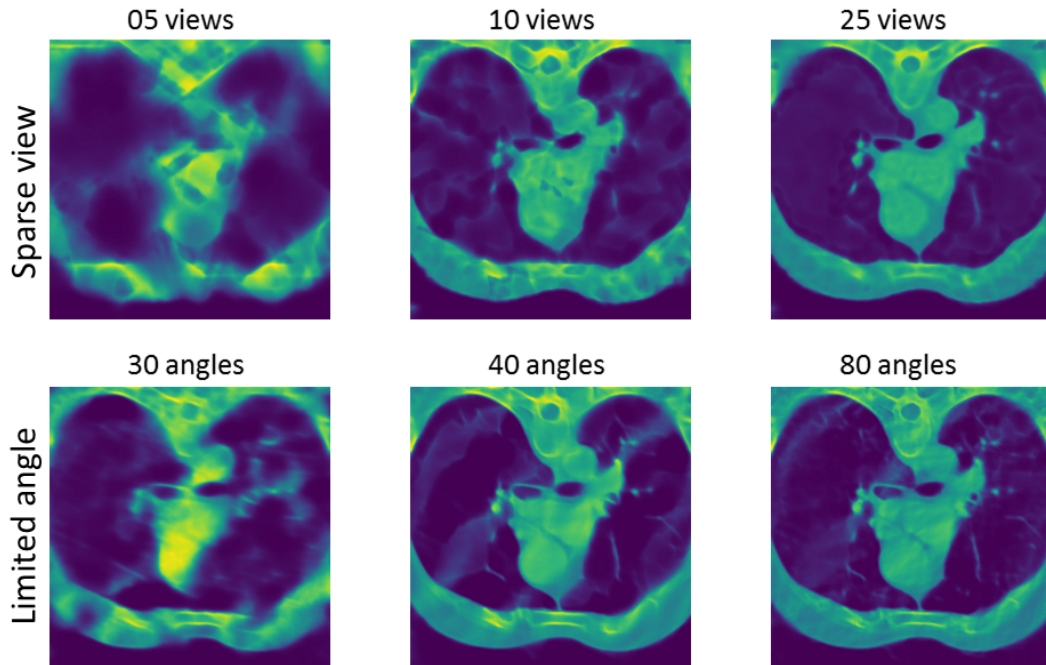
Figure 5. Different challenging reconstructions of the LoDoPaB-CT dataset with IntraTomo. The first row corresponds to sparse view reconstruction with a different number of sparse views: 5, 10 and 20 (from left to right). In the second row, limited angle tomographic reconstruction results are shown for the cases of 30, 40 and 80 degrees (from left to right).
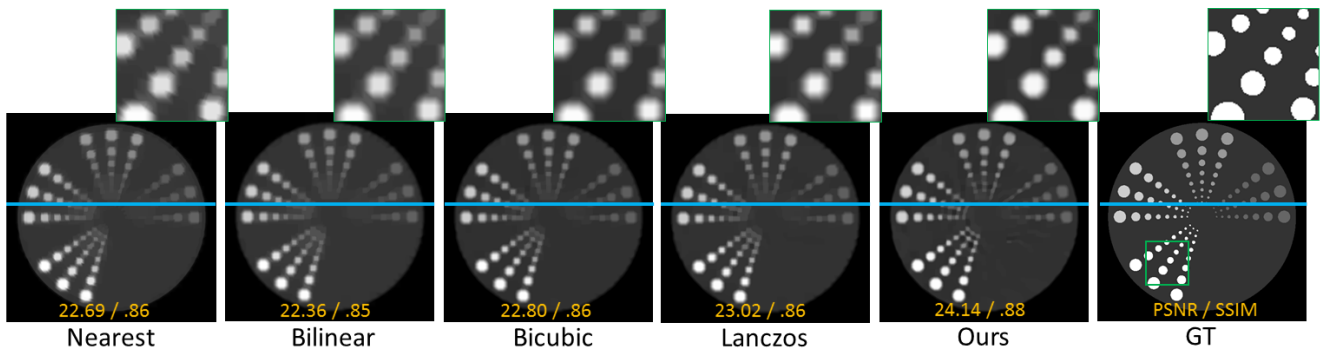

Figure 6. Examples of super-resolution tomography. From left to right: a Nearest, Bilinear, Bicubic, Lanczos upsampling of low-resolution sinograms with ROF reconstruction [6], ours (IntraTomo), and GT, respectively. The (PSNR(dB)/ SSIM) measurements are given for each approach on the image.

References

[1] A. H. Andersen and A. C. Kak. Simultaneous algebraic reconstruction technique (SART): a superior implementation of the ART algorithm. *Ultrasonic imaging*, 6(1):81–94, 1984. 2, 3

[2] A. Chambolle, M. J. Ehrhardt, P. Richtárik, and C.-B. Schonlieb. Stochastic primal-dual hybrid gradient algorithm with arbitrary sampling and imaging applications. *SIAM Journal on Optimization*, 28(4):2783–2808, 2018. 1, 2, 3

[3] C. A. Cocosco, V. Kollokian, R. K.-S. Kwan, G. B. Pike, and A. C. Evans. Brainweb: Online interface to a 3D MRI simulated brain database. In *NeuroImage*. Citeseer, 1997. 1, 3

[4] F. De Carlo, D. Gürsoy, D. J. Ching, K. J. Batenburg, W. Ludwig, L. Mancini, F. Marone, R. Mokso, D. M. Pelt, J. Sijbers, et al. TomoBank: a tomographic data repository for computational x-ray science. *Measurement Science and Technology*, 29(3):034004, 2018. 1, 3, 5, 6

[5] M. Gadelha, R. Wang, and S. Maji. Shape reconstruction using differentiable projections and deep priors. In *Proc. ICCV*, pages 22–30,
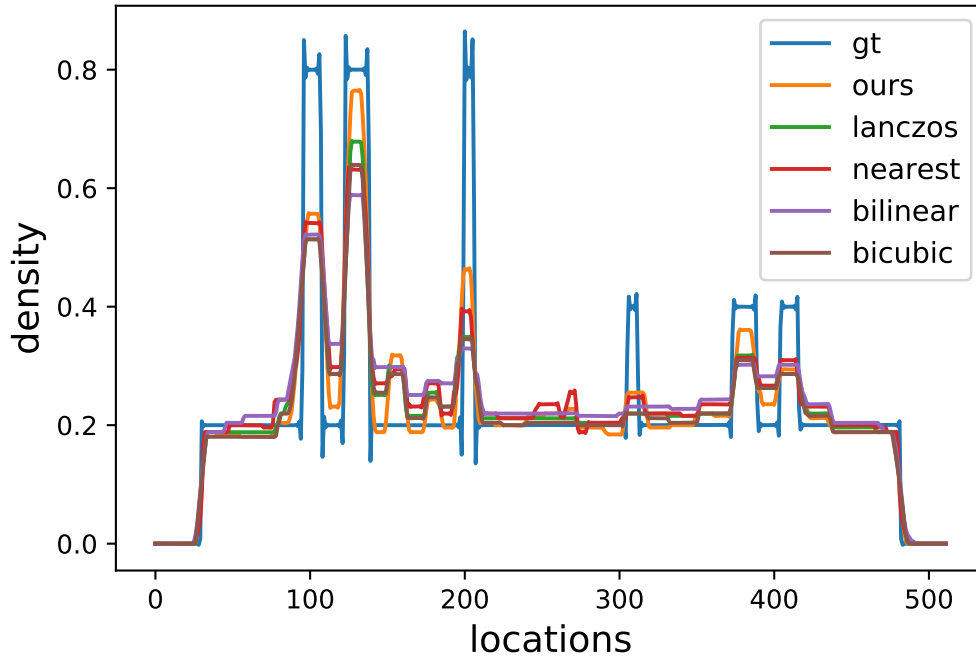
Figure 7. Super-resolution tomography with 1D scan-line of reconstructed density field (the blue lines on super-resolution results in Figure 6) with different interpolation techniques.
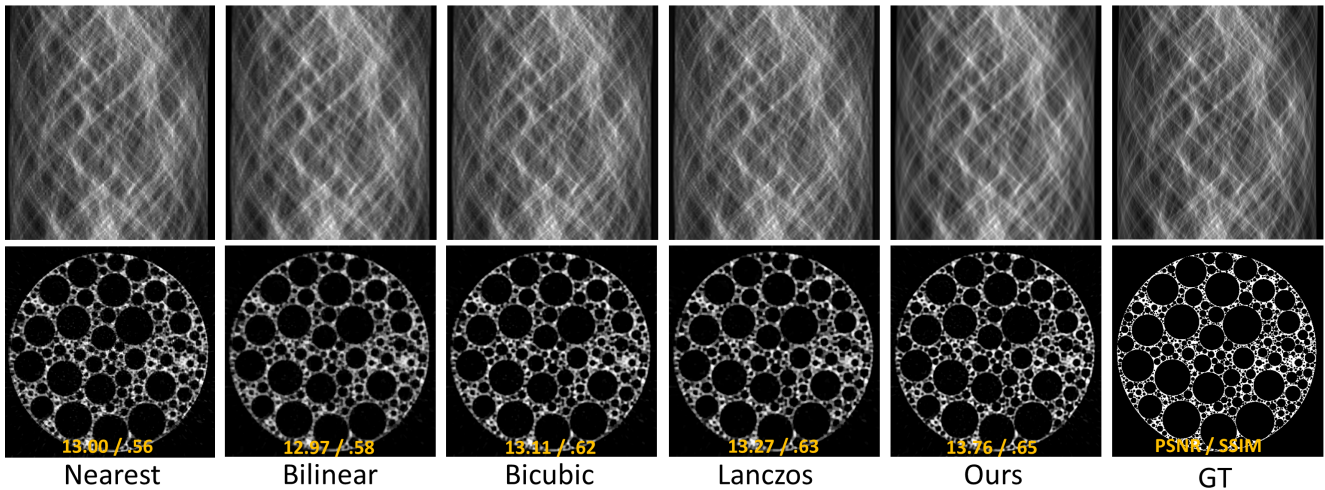

Figure 8. Super-resolution tomography (4 times upsampling) with Foam phantom [4]. From left to right: a Nearest, Bilinear, Bicubic, Lanczos upsampling of low-resolution sinogram with ROF reconstruction [6], ours (IntraTomo), and GT, respectively. The (PSNR(dB)/ SSIM) measurements are given for each approach on the image.

2019. 2, 3, 6

[6] P. Getreuer. Rudin-Osher-Fatemi total variation denoising using split Bregman. *Image Processing On Line*, 2:74–95, 2012. 2, 3, 4, 5, 6

[7] S. A. Harmon, T. H. Sanford, S. Xu, E. B. Turkbey, H. Roth, Z. Xu, D. Yang, A. Myronenko, V. Anderson, A. Amalou, et al. Artificial intelligence for the detection of COVID-19 pneumonia on chest CT using multinational datasets. *Nature communications*, 11(1):1–7, 2020. 1, 3
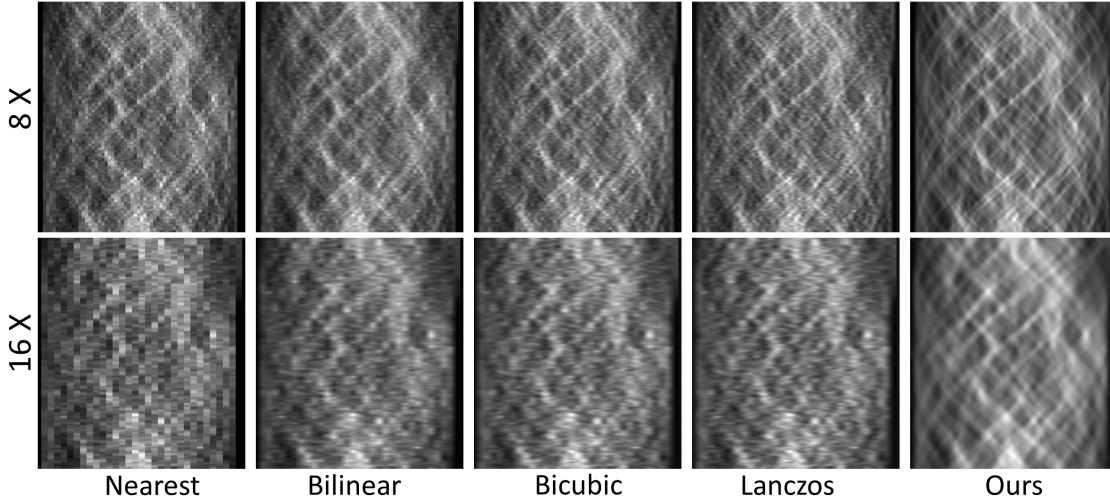
Figure 9. Examples of super-resolution tomography with Foam phantom [4]. The projections are upsampled with 8 (first row) and 16 (second row) with different approaches, respectively.

		Deep prior [5]	IntraTomo (Ours)
	10	23.95/ .95	25.67/ .97
Sparse view tomography	**15**	27.32/ .97	30.40/ .98
	20	27.61/ .97	32.36/ .99
	25	28.86/ .98	34.70/ .99
		Deep prior [5]	**IntraTomo (Ours)**
	20	15.37/ .67	19.68/ .88
Limited angle tomography	**30**	16.07/ .72	23.58/ .95
	45	17.05/ .78	25.33/ .97
	60	18.12/ .83	28.40/ .98
		Lanczos (ROF) [6]	**IntraTomo (Ours)**
Super resolution tomography	**2X**	32.33/ .95	32.66/ .95
	4X	28.28/ .88	28.82/ .89
	8X	21.80/ .77	22.48/ .78

Table 4. Comparative study. PSNR/SSIM measurements for different conditions in sparse view tomography, limited angle tomography, and super resolution tomography with Pepper dataset. Higher values are better for PSNR and SSIM.

[8] K. H. Jin, M. T. McCann, E. Froustey, and M. Unser. Deep convolutional neural network for inverse problems in imaging. *IEEE Trans. Image Proc.*, 26(9):4509–4522, 2017. 3

[9] J. Leuschner, M. Schmidt, D. O. Baguer, and P. Maaß. The lodopab-ct dataset: A benchmark dataset for low-dose ct reconstruction methods. *arXiv preprint arXiv:1910.01113*, 2019. 1, 3

[10] S.-L. Liew, J. M. Anglin, N. W. Banks, M. Sondag, K. L. Ito, H. Kim, J. Chan, J. Ito, C. Jung, N. Khoshab, et al. A large, open source dataset of stroke anatomical brain images and manual lesion segmentations. *Scientific data*, 5(1):1–11, 2018. 1, 3
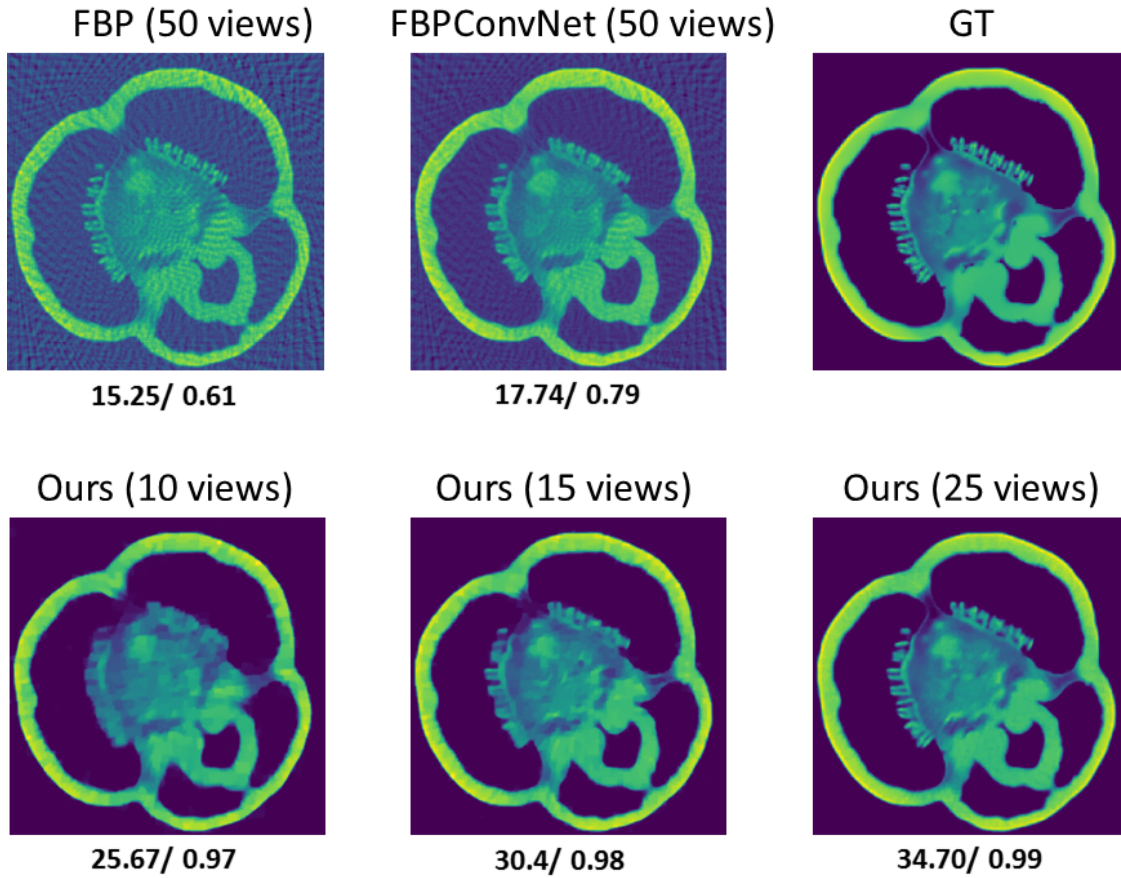
Figure 10. A comparison between FBP method, FBPConvNet, and ours for pepper data.

[11] X. Pan, E. Y. Sidky, and M. Vannier. Why do commercial CT scanners still employ traditional, filtered back-projection for image reconstruction? *Inverse problems*, 25(12):123009, 2009. 2, 3

[12] L. A. Shepp and B. F. Logan. The Fourier reconstruction of a head section. *IEEE Transactions on nuclear science*, 21(3):21–43, 1974. 1, 2, 3

[13] W. Van Aarle, W. J. Palenstijn, J. Cant, E. Janssens, F. Bleichrodt, A. Dabravolski, J. De Beenhouwer, K. J. Batenburg, and J. Sijbers. Fast and flexible X-ray tomography using the ASTRA toolbox. *Optics express*, 24(22):25129–25147, 2016. 1
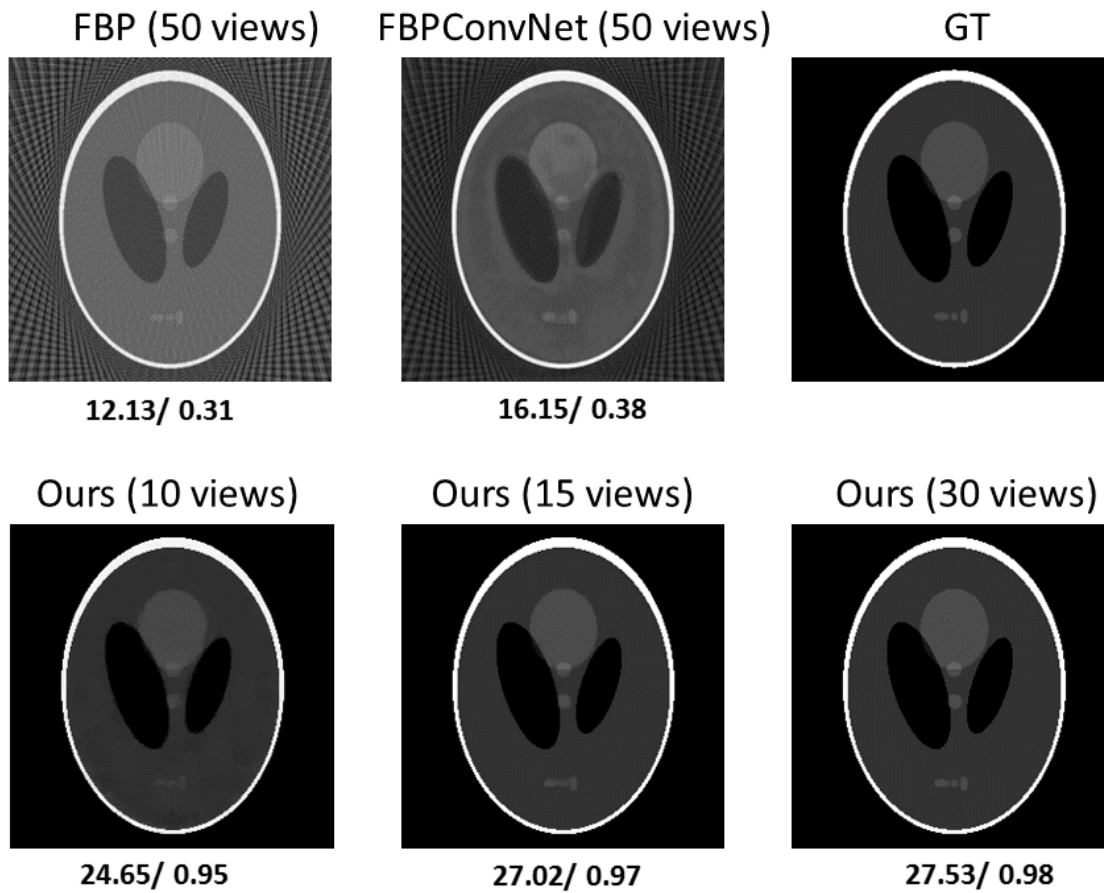
Figure 11. A comparison between FBP method, FBPConvNet, and ours for Shepp-Logan phantom.